Tensor gradiometry with a diamond magnetometer

A.J. Newman,[1,2,*] S.M. Graham,[1,2] A.M. Edmonds,[3] D.J. Twitchen,[3] M.L. Markham,[3] and G.W. Morley[1,2,†]

[1] *Department of Physics, University of Warwick, Gibbet Hill Road, Coventry CV4 7AL, United Kingdom*
[2] *EPSRC Centre for Doctoral Training in Diamond Science and Technology, University of Warwick, Coventry CV4 7AL, United Kingdom*
[3] *Element Six Innovation, Harwell Oxford, Fermi Avenue, Didcot OX11 0QR, United Kingdom*

(Received 6 August 2023; revised 6 September 2023; accepted 13 December 2023; published 3 January 2024)

Vector magnetometry provides more information than scalar measurements for magnetic surveys utilized in space, defense, medical, geological, and industrial applications. These areas would benefit from a mobile vector magnetometer. Here we present a scanning fiber-coupled nitrogen-vacancy (N-*V*) center vector magnetometer. Feedback control of the microwave excitation frequency is used to improve dynamic range and maintain sensitivity during movement of the sensor head. Tracking of the excitation frequency shifts for all four orientations of the N-*V* center allows us to image the vector magnetic field of a damaged steel plate. We calculate the magnetic tensor gradiometry images in real time, and they allow us to detect smaller damage than is possible with vector or scalar imaging.

DOI: 10.1103/PhysRevApplied.21.014003

I. INTRODUCTION

Tensor gradiometry calculates the gradient of all three components of a vector in all three directions [1–3]. At each point in space, magnetic tensor gradiometry measures

$$\begin{bmatrix} B_{xx} & B_{xy} & B_{xz} \\ B_{yx} & B_{yy} & B_{yz} \\ B_{zx} & B_{zy} & B_{zz} \end{bmatrix} = \begin{bmatrix} \frac{\partial B_x}{\partial x} & \frac{\partial B_y}{\partial x} & \frac{\partial B_z}{\partial x} \\ \frac{\partial B_x}{\partial y} & \frac{\partial B_y}{\partial y} & \frac{\partial B_z}{\partial y} \\ \frac{\partial B_x}{\partial z} & \frac{\partial B_y}{\partial z} & \frac{\partial B_z}{\partial z} \end{bmatrix}. \quad (1)$$

This technique, also called full tensor gradiometry, can provide benefits over vector measurements including improvements to spatial resolution [4–6], directional filtering [7], common mode noise rejection [8,9], and decoupling the contributions from homogeneous background fields [10–12]. Gradients due to local anomalies are larger than homogeneous background fields, and therefore smaller features can be resolved where normally they would be dominated by the larger background.

Measuring the magnetic field components around an ensemble of nitrogen-vacancy (N-*V*) centers in diamond can provide vector information instead of just the scalar projection along one of the four possible N-*V* center axes in the diamond [13]. N-*V* vector magnetometry takes advantage of using the magnetic sensitivity of all four possible orientations of the defect rather than just a single orientation, increasing the probe population by four. Vector measurements are important in applications such as magnetic navigation [14], battery monitoring [15,16], unexploded ordnance detection [17], space missions, and geological surveys [11,18–20] and could be applied to areas such as archaeology, nondestructive testing [21], magnetocardiography [22], magnetoencephalography [23–27], and nuclear magnetic resonance spectroscopy [28]. Magnetic imaging of damage in steel is of great interest to industry [21,29–36].

Magnetic sensing is possible with N-*V* centers in diamond through optically detected magnetic resonance (ODMR). Magnetometry with N-*V* centers provides high dynamic range and has previously demonstrated, in other work, the ability to perform measurements in a wide temperature range, in chemically harsh environments, and under high irradiation [37–39]. Ensembles of N-*V* centers provide high magnetic sensitivities, with small sensing volumes, e.g., 1 mm^3 or less [40–50]. N-*V* center magnetometers have shown a range of applications including sensing induced eddy currents [51–53], single-neuron action potentials [54], and magnetic nanoparticle sensing in biomedical tissue [55,56].

*Alex.Newman@warwick.ac.uk
†Gavin.Morley@warwick.ac.uk

Vector magnetometry with N-V centers uses excitation of the ground-state spin-level transition $m_s = 0 \rightarrow m_s = \pm 1$ for at least three of the four possible orientations of the N-V centers in diamond. This enables vector magnetometry with N-V centers using a single sensor head, unlike other magnetometers such as fluxgates that require multiple sensors. This means that low nonlinearity and nonorthogonality are built in. A majority of high-sensitivity N-V center magnetometers are tabletop setups, which are immobile preventing them from being used for scanning over a sample of interest.

In recent years fiber-coupled diamond magnetometers using both single and ensemble N-V centers have demonstrated subnanotesla sensitivities [57–62]. Diamond-based fiber-coupled magnetic gradiometers have also been demonstrated previously either using two spatially separated diamonds [63] or using two fibers to probe two distinct areas on a single diamond [64].

Our fiber-coupled N-V magnetometer setup can take vector measurements while scanning through three-dimensional (3D) space, rather than being fixed at a single point in space, allowing magnetic tensor gradiometry images to be recorded. A small magnet injects magnetic flux into the sample to be imaged, and distortions of this flux by the sample are imaged by the diamond magnetometer [21].

Here we present a scanning fiber-coupled N-V magnetometer that is capable of both vector magnetometry and magnetic tensor gradiometry with a moving sensor head, independent of the main optoelectronics housed in a mobile equipment rack. Changes in the ODMR peak frequencies from magnetic field perturbations are tracked to calculate magnetic field vectors and gradients, while simultaneously moving the sensor head through the environment. As a demonstration of its capabilities, magnetic vector measurements around a 316 stainless steel plate [Fig. 1(a)] are made. The plate has holes drilled in at various positions with a range of sizes to simulate damage. We use no magnetic shielding.

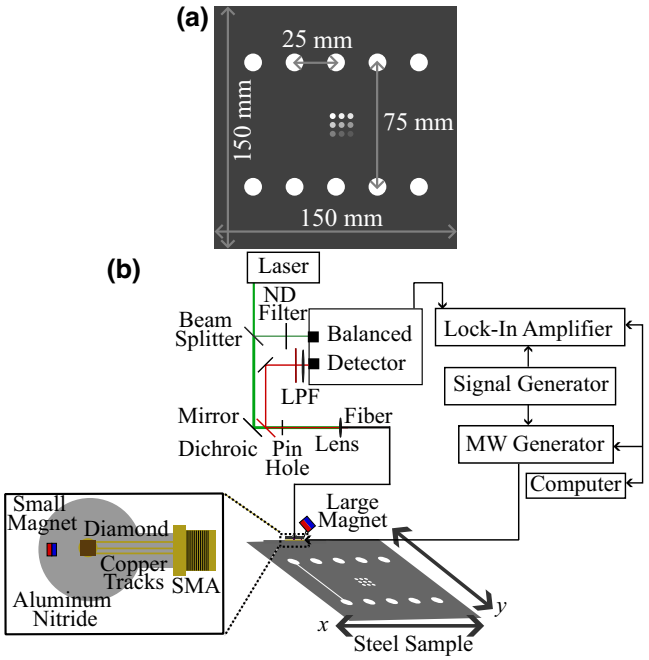

FIG. 1. (a) The 4.5-mm 316 steel plate used in this work. The large holes have a diameter of 6 mm and the small holes have a diameter of 2 mm with a separation of 10 mm. The small holes are drilled at varying depths from 4.5 mm (top left) to 0.5 mm (bottom right). (b) Diagram of the scanning magnetometry setup (ND, neutral density; MW, microwave; LPF, low-pass filter). The diamond sits on top of the microwave loop, which is printed onto an aluminum nitride base.

II. EXPERIMENTAL DETAIL AND METHOD

The fiber-coupled scanning setup is shown in Fig. 1(b). A Laser Quantum 532-nm GEM laser is used for excitation of the N-V ensemble of the diamond, inside the sensor head. A laser power of 1 W is used with approximately 0.6 W of power measured at the diamond. The optoelectronics are kept on a mobile rack, which allows for more portability. The fiber is a custom-ordered FG910UEC 3-m fiber with a core diameter of 0.91 mm with steel ferrule-connector-physical-contact (FCPC) connectors on both ends. The fiber is directly coupled to the diamond on the sensor head via an SM1FC2 fiber adapter, which is then screwed down onto the antenna substrate to make contact with the diamond. The fiber is secured to reduce modal noise from movement of the fiber during scanning of the sensor head. Fluorescence from the sensor head is sent back through the same fiber and separated via a dichroic mirror (Thorlabs DMSP650) to be focused, by an aspheric lens through a long-pass filter, onto one of the two photodiodes on a Thorlabs PD450A balanced detector. The other photodiode takes a reference beam directly from the green laser, which allows for cancellation of common mode noise, mainly laser noise. When the sensor head is on resonance, the reference and fluorescence signals are balanced to get the best cancellation performance. The subtracted signal from the output of the balanced detector is then digitized and demodulated via a Zurich MFLI DC 500-kHz lock-in amplifier (LIA).

Microwaves are provided by an Agilent E8257D microwave source and amplified via a 43-dB Mini-Circuits ZHL-16W-43-S+. Microwaves are delivered to the diamond by a 2-m coaxial cable, which connects to an SubMiniature version A (SMA) adapter soldered directly to a coplanar waveguide on an aluminum nitride ceramic printed circuit board. The waveguide then leads to a 3.0-mm-diameter loop antenna with the diamond situated in the center. The aluminum nitride provides high thermal conductivity to act as a good heat sink, pulling heat from the diamond as it is heated by both the laser and

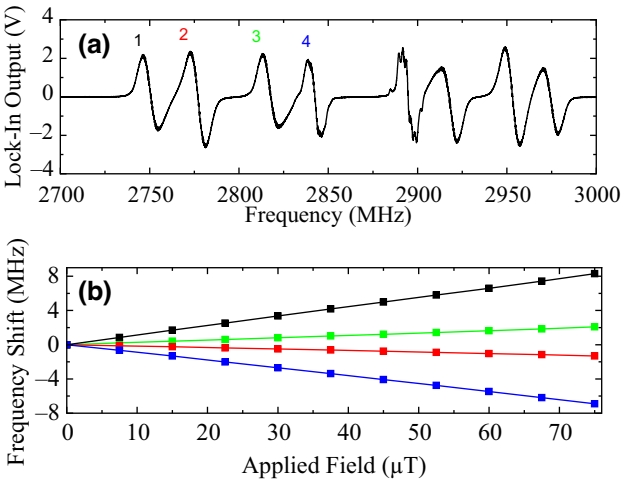

FIG. 2. (a) Optically detected magnetic resonance spectrum used for vector measurements while the sensor head is on the steel. (b) Example of tracked frequency shifts of four peaks, as labeled in (a), as an applied solenoid field along the z axis is increased.

microwaves. The diamond is a 1-mm cube. It is a low-strain diamond grown with chemical vapor deposition by Element Six, having (100) polished faces and 99.995% ^{12}C isotopic purification [65].

A permanent Nd-Fe-B magnet is attached to the side of the sensor head using a custom 3D-printed mount, which allows 360° rotation around the azimuthal angle and 180° rotation in the polar angle. The magnet is orientated until the bias field projection differs for all four crystallographic directions of the N-V center, to provide all eight separate resonance peaks in the ODMR spectrum, as seen in Fig. 2(a). Parameter optimization is performed to achieve the best sensitivity for vector magnetometry, following the process outlined in Ref. [66]. With a low-pass filter with a 150-Hz 3-dB point, the optimum parameters for microwave power after the amplifier, modulation frequency, and modulation amplitude are found to be 30 dBm, 3.0 kHz, and 3.0 MHz, respectively. The microwaves are sine wave frequency modulated. To determine the sensitivity during optimization, a linear fit is made to the fourth ODMR peak [Fig. 2(a)] and then fast Fourier transforms (FFTs) of thirty 1-s time traces are taken and averaged, when on the central frequency of that peak. The mean sensitivity is taken as the average value between 10 and 150 Hz, excluding the 50-Hz peak due to the mains electricity.

A 3D printer stage is used to scan the sensor head in three axes. The stage allows for control over the step size and speed of the scan as well as the lift-off distance in the z axis. The step size used for the x and y movement was 0.5 mm.

III. RESULTS

Changes to the external magnetic field are measured by looking at the change in peak resonance frequency due to Zeeman shift of the N-V center $m_s = -1$ spin level. The shift in resonance frequency causes the fluorescence intensity to change, which results in a change in the LIA voltage output. When scanning over a magnetic object, like the steel plate, the change in external field is caused by the difference in the amount of material near the sensor head. The changes in voltage are used to provide a process variable for a proportional linear feedback system, which adjusts the microwave frequency to continually follow the central frequencies of the four chosen peaks. Using the peak's central resonance frequency as a set point, any changes to the continually monitored voltage while at that central frequency can be used to determine the shift in resonance frequency, by using the known gradient of the ODMR peak. The calculated shift in resonance is used as an error signal that is sent to the microwave source to change the microwave frequency until the monitored voltage returns to its set-point value, at the center of the peak. This is then expanded to cover four ODMR peaks by sequentially looping over each one, approximately every 70 ms, to measure their individual shifts, as shown in Fig. 2(b). Tracking the four peaks can then be used to determine the magnetic field shift components along each of the four N-V center axes, which ultimately allows for calculation of the B_x, B_y, and B_z components of the field, relative to a coordinate frame defined around the sensor head. These measurements are the change in magnetic field relative to the background field from our bias magnets. Another advantage to this resonance tracking technique is that it provides a much higher dynamic range of the magnetometer as the sensitive range is no longer limited to the linewidth, or linear region, of the ODMR peak.

The vector components of an applied field are reconstructed using four ODMR line centers, which each represent the four possible orientations of the N-V center. The first four ODMR line centers used represent the $m_s = 0$ to $m_s = -1$ transitions of the four orientations [Fig. 2(a)]. The method to calculate the vector components is taken from the work done by Schloss *et al.* [13]. The linearized N-V center ground-state Hamiltonian allows magnetic field components to be determined from the frequency shifts of the four peaks. The result is

$$\begin{bmatrix} B_x \\ B_y \\ B_z \end{bmatrix} = \mathbf{A}^{-1} \begin{bmatrix} \Delta f_1 \\ \Delta f_2 \\ \Delta f_3 \\ \Delta f_4 \end{bmatrix}, \quad \mathbf{A} = \begin{bmatrix} \frac{\partial f_1}{\partial B_x} & \frac{\partial f_1}{\partial B_y} & \frac{\partial f_1}{\partial B_z} \\ \frac{\partial f_2}{\partial B_x} & \frac{\partial f_2}{\partial B_y} & \frac{\partial f_2}{\partial B_z} \\ \frac{\partial f_3}{\partial B_x} & \frac{\partial f_3}{\partial B_y} & \frac{\partial f_3}{\partial B_z} \\ \frac{\partial f_4}{\partial B_x} & \frac{\partial f_4}{\partial B_y} & \frac{\partial f_4}{\partial B_z} \end{bmatrix}, \tag{2}$$

where Δf_i is the shift in frequency of peak $i = 1, 2, 3, 4$ and $\mathbf{A^{-1}}$ is the psuedoinverse of matrix $\mathbf{A}$ where B_x, B_y, and B_z are the magnetic field components in the frame defined around the sensor head.

To calculate matrix $\mathbf{A}$, first the sensor head was placed inside a Helmholtz coil with a calibration of 78.2 μT/A between 0.1 and 1 A. The calibration was performed with a Bartington Instruments Mag-03MS100 three-axis fluxgate magnetometer. The coil was aligned along the defined x axis relative to the sensor head and the peak shifts were tracked as the current was increased in steps of 0.1 A. This was repeated for the y and z axes. A linear fit for all four peaks for each axis orientation was made to determine the change in peak central frequency with the increase in applied field, as shown in Fig. 2(b). The matrix $\mathbf{A}$, from the 12 fits, was found to be

$$\mathbf{A}\ (\mathrm{MHz}/\mu\mathrm{T}) = \begin{bmatrix} 0.12 & 0.04 & -0.13 \\ -0.02 & -0.10 & -0.09 \\ 0.03 & 0.11 & -0.19 \\ -0.09 & -0.03 & -0.14 \end{bmatrix}. \quad (3)$$

With this calibration matrix it is then possible to track the peak shifts and calculate the vector components of the field that caused said shift. We do this in real time.

A (160 × 160)-mm^2 scan was done across the (150 × 150)-mm^2 316 stainless steel plate, with a step size of 0.5 mm for both the x and y directions and with a separation distance of approximately 1 mm between the surface of the steel sample and the base of the antenna. The antenna is 1-mm thick so the sensing diamond is 2 mm away from the sample. A map of the magnitude of the shifts of the field components is produced by using $f = \sqrt{B_x^2 + B_y^2 + B_z^2}$. This is not the same as the total magnetic intensity $||\mathbf{B}|| = \sqrt{(B_x + B_x^{\mathrm{bias}})^2 + (B_y + B_y^{\mathrm{bias}})^2 + (B_z + B_z^{\mathrm{bias}})^2}$ or the shift in total magnetic intensity due to the fact that the shift in field components is being measured and not the absolute value.

Both the large and small holes are successfully imaged in all three vector components; an example of B_x is shown in Fig. 3(a). The features are also clearly visible in Fig. 3(b), where the change in f indicates a lack of steel. With the addition of vector magnetometry we are also able to plot the magnetic field shift vectors, which can help with locating and analyzing defects, as shown in Fig. 3(c). The magnetic field preferentially flows through the higher-permeability steel, as opposed to the air and this can be visualized with the field shift vectors as they move away and around the hole feature in the map to stay flowing through the steel.

Two horizontal lines of evenly spaced quadrupole shapes at the top and bottom of the plate indicate the locations of the large holes in the steel, with the grid of nine holes in the center. The quadrupole field shape coming from the holes [Figs. 3(c) and 4(a)] is found to be due to the orientation of the small bias magnet relative to the hole features. Rotating the magnet 45°, between having its square face facing the diamond and having it edge-on to the diamond, produces different field shift component images, as seen in Fig. 4(b), where the B_x field shift component now has a more dipolelike shape. By performing COMSOL simulations, it is verified that the rotation of the small bias magnet is the cause of the change in field pattern seen. Simulations of a 316 stainless steel plate with a 6-mm hole and a 1-mm-cube 0.1-T permanent magnet placed 1 mm above the hole match well with what is measured when the magnet is not rotated [Fig. 4(c)] and with a rotation of 45° [Fig. 4(d)].

Scanning vector magnetometry makes it possible to perform tensor gradiometry. We have three matrices each containing the B_x, B_y, and B_z field components at different adjacent x, y, and z positions so we can take the gradient of the field components with respect to the three Cartesian directions and generate nine tensor components for each point in space.

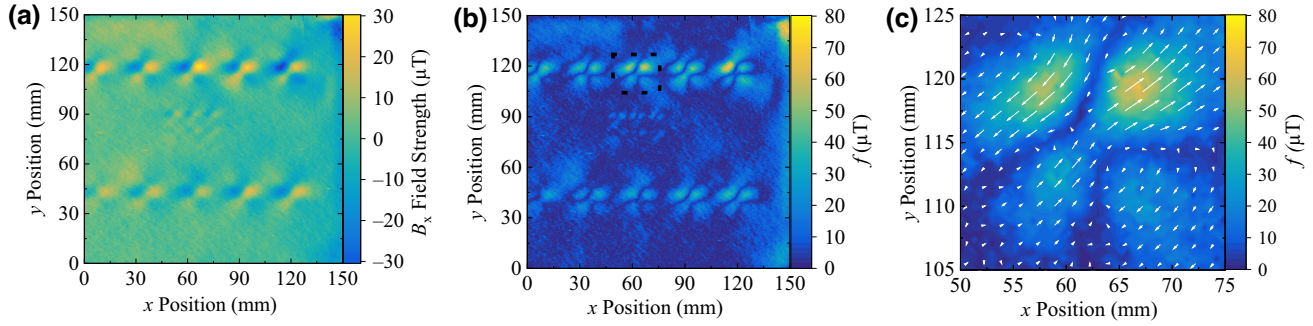

FIG. 3. (a) Map of the B_x field strength. (b) Map of the magnitude of shifts, $f = \sqrt{B_x^2 + B_y^2 + B_z^2}$. The highlighted box shows a region where a 6-mm hole is located. (c) Measured magnetic field shift vectors from the highlighted region. Collecting these images took 12 h, which is nine times faster than in Ref. [21], due to reduced dwell time before moving to the next pixel.

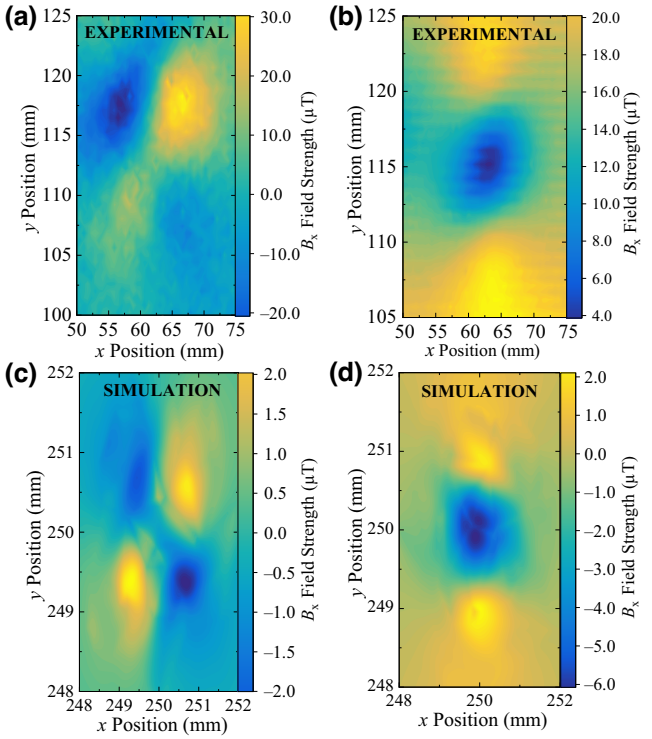

FIG. 4. (a) B_x field component image over a single 6-mm-diameter hole for the unrotated small bias magnet, showing quadrupole pattern. (b) B_x field component image over a single large hole for the rotated small bias magnet, showing dipole pattern. (c) COMSOL simulation of the B_x field over a large hole with an unrotated magnet. (d) COMSOL simulation of the B_x field over a large hole with a rotated magnet.

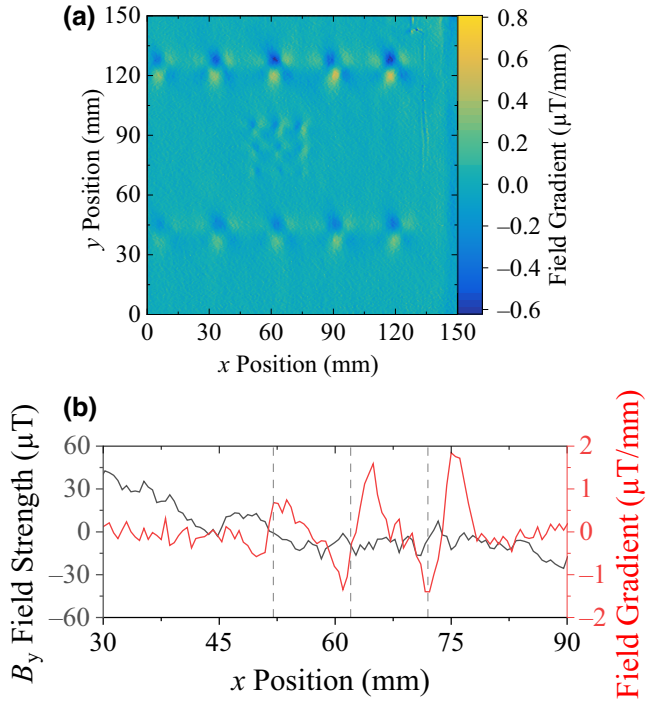

FIG. 5. (a) B_{xy} tensor component map. (b) A $y = 97$-mm horizontal line profile over top row of central small 2-mm-diameter holes, for both the B_y component (black) and the B_{xy} component (red).

An example of this can be seen in Fig. 5(a) where the B_{xy} tensor component from Eq. (1) has been plotted and it is clear that some features, for example the three lowest holes in the smaller grid of nine 2-mm holes in the center of the plate, are shown more clearly when compared with the magnitude map [Fig. 3(b)] and B_x map [Fig. 3(a)] where the three lowest of the smaller central holes are virtually impossible to resolve. The tensor components for the change in z direction were also calculated but did not provide any useful information: for more on this, see the Appendix I. To compare this with the B_x map, a horizontal line profile on the B_{xy} map [Fig. 5(a)] is taken across the small holes at the same y positions as on the B_x map.

In conclusion, magnetic tensor gradiometry was shown to improve the imaging of small holes in steel, making them easier to characterize. This technique, with further optimization, could detect subsurface magnetic anomalies or magnetic fields from sources behind nonmagnetic insulating layers with better spatial resolution. Optimization of the tensor gradiometry measurements could also provide inherent directional filtering to help with determining the boundaries between magnetic field sources and the location of individual magnetic domains. Imaging other magnetic samples that are not steel could be of interest such as batteries [15,16] and current-carrying wires [67].

Further improvements to the system could include using four frequencies simultaneously with no hopping so that the four resonance frequencies could be addressed simultaneously to remove the delay in switching between them [13]. The removal of this delay would increase the speed at which the tracking reacts and therefore allow for measurements of faster-changing fields. With a faster-reacting feedback system, it would be then possible for the sensor head to be moved rapidly through its environment, such as being handheld and scanned over objects, making it more applicable for in-the-field measurements and more widely applicable in the areas of industry previously discussed. Calibration of the sensor head requires a test field to be applied along the three defined axes. By using a three-axis Helmholtz coil, test fields could be applied more accurately along the three axes, reducing the nonlinearity and nonorthogonality response from each direction.

ACKNOWLEDGMENTS

The authors thank Jeanette Chattaway, Lance Fawcett, and Matty Mills of the Warwick Physics mechanical workshop. We are grateful for insightful discussions with Rajesh Patel throughout this work. A.J.N.'s Ph.D. studentship is funded by an EPSRC iCASE award to

NNL (the National Nuclear Laboratory). S.M.G.'s Ph.D. studentship is funded by DSTL (the Defence Science and Technology Laboratory). This work is supported by the UK Networked Quantum Information Technologies (NQIT) Hub, and the UK Hub in Quantum Computing and Simulation, part of the UK National Quantum Technologies Programme, with funding from UKRI EPSRC Grants No. EP/M013243/1 and No. EP/T001062/1, respectively. This work is also supported by Innovate UK Grant No. 10003146, EPSRC Grant No. EP/V056778/1, and an EPSRC Impact Acceleration Account (IAA) award. G.W.M. is supported by the Royal Society.

APPENDIX A: PHYSICS OF THE NITROGEN-VACANCY CENTER

The N-V center is a color center in diamond, which is made up of a substitutional nitrogen atom, replacing a carbon atom in the diamond lattice, adjacent to a vacancy [46]. The defect has trigonal symmetry with four possible orientations in the lattice: [111], [$\bar{1}\bar{1}$1], [1$\bar{1}\bar{1}$], and [$\bar{1}$1$\bar{1}$]. The negative charge state of the N-V center is a spin-1 defect with a spin-triplet ground and excited state (Fig. 6). The spin state can be polarized and read out using ODMR. The N-V center can be polarized to the $m_s = 0$ sublevel of the $^3A_2$ ground state with a 532-nm laser. Population in the $m_s = \pm 1$ sublevels has an increased chance of relaxing through the singlet states nonradiatively via intersystem crossing. The spin state of the N-V center can then be read out from the change in fluorescence intensity. The spin state can be driven from the $m_s = 0$ to the $m_s = \pm 1$ sublevels using microwaves. The zero-field splitting of the ground state is approximately 2.87 GHz at room temperature but after an external magnetic field is applied, Zeeman splitting of the $m_s = \pm 1$ sublevels occurs and two transitions form at two different frequencies. The splitting of these frequencies is

$$\Delta f = 2\gamma B_{\text{N-}V}, \tag{A1}$$

where $B_{\text{N-}V}$ is the external field projected along the N-V center axis for one of the four allowed orientations and $\gamma = 28$ GHz/T is the gyromagnetic ratio of the N-V center. Further splitting, from hyperfine interactions, occurs between the $S = 1$ electron spin and the $I = 1$ nuclear spin of the ^{14}N atom of the N-V center. Each resonance is split into three separated by approximately 2.158 MHz.

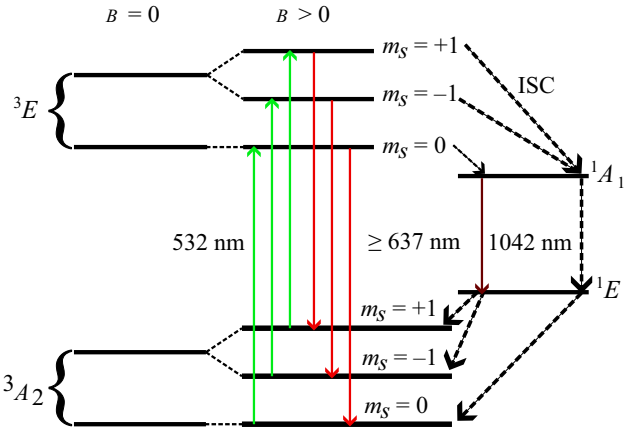

FIG. 6. Nitrogen-vacancy center energy level diagram, with electric dipole transitions and intersystem crossing (ISC).

APPENDIX B: DIAMOND PROPERTIES

A (2.97 × 2.93 × 0.93)-mm^3 CVD diamond was laser cut into nine 1-mm^3 diamonds, one of which is used in this work. The diamond is isotopically purified 99.995% ^{12}C to minimize the concentration of ^{13}C with $I = 1/2$ nuclear spin [65]. The diamond was electron-irradiated and annealed to increase the N-V center population, which was determined to be approximately 2.8 ± 0.2 parts per million by electronic paramagnetic resonance (EPR) measurements using a Bruker EMX spectrometer with a 90-dB microwave bridge and a Bruker super-high-Q cavity. T_2^*, T_2, and T_1 times of 750 ns, 1.3 μs, and 5.1 ms were measured respectively from pulsed EPR measurements. From the measured T_2^* time, a calculated 0.42-MHz minimum ODMR linewidth is possible. Microwave and laser power broadening as well as bias field inhomogeneities cause the ODMR spectrum to be broader than this value. Growth, irradiation, annealing, and polishing were done b y Element Six.

APPENDIX C: SENSOR HEAD

Figure 7 shows the cross section of the sensor head used in this work, including the aluminum substrate and transmission lines. A Thorlabs SM1FC fiber adapter is used to mount the fiber to the antenna substrate to which the custom patch fiber is connected via a steel FCPC connector. The adapter is screwed down to make physical contact with the diamond on the board for direct fiber coupling. The small 1-mm^3 Nd-Fe-B permanent magnet is shown next to the diamond. The sensor head is 45 mm in diameter and 8 mm in height, with an extra 8-mm-long rectangle on the side to allow an SMA adapter to be soldered on. The diamond is held in place at the center of the antenna loop,

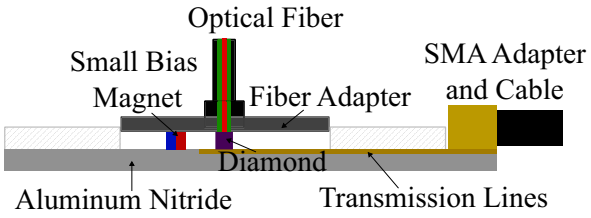

FIG. 7. Cross section of the sensor head.

which has microwaves sent to it via transmission lines. The aluminum nitride substrate thickness gives a minimum diamond-to-sample distance of 1 mm.

APPENDIX D: MAGNETOMETER SENSITIVITY

Two key factors that affect the sensitivity of the magnetometer are the gradient of the ODMR peak and the level of the noise floor. By increasing the gradient, a larger change in voltage is seen for a particular field strength and so weaker fields can still be determined. By reducing the overall noise floor, the signal strength required to discern noise from a magnetic field signal is reduced, and therefore weaker fields can be detected. The gradients are found from linear fits to the first four peaks as seen in Fig. 8. This gradient then allows conversion of voltage into magnetic field, using the gyromagnetic ratio, which is used along with thirty 1-s FFTs, taken by a PicoScope 5442D at a sampling rate of 10 kHz, to produce a spectral density graph where the average value in the region of interest (10–100 Hz, excluding only the 50-Hz mains peak) is taken as the sensitivity. The sensitivity error is taken as the standard deviation of this region. The FFTs taken were put through a Blackman window and amplitude corrected. The FFTs are converted from decibel units (dBu), referenced to 0.775 V_{rms}, to volt units using the conversion of $0.775 \times 10^{L/20}$, where L is the noise floor of the FFT in dBu. The gradients for the peaks can then be used to convert the FFTs into units of $\mathrm{nT}/\sqrt{\mathrm{Hz}}$.

Figure 8 shows the ODMR spectrum for each of the four peaks, with the sensor head on the steel plate. The sensitivity achieved for peaks 1 to 4, respectively, is 3.3 ± 1.7, 5.2 ± 1.7, 3.6 ± 2.5, and 9.5 ± 5.3 $\mathrm{nT}/\sqrt{\mathrm{Hz}}$, without frequency hopping (Fig. 9). The photon shot noise was calculated to be 620 $\mathrm{pT}/\sqrt{\mathrm{Hz}}$.

To determine how sensitive the magnetometer is along the B_{x}, B_{y}, and B_{z} axes, thirty 1-s time traces were taken on resonance for each of the four ODMR peaks, and then

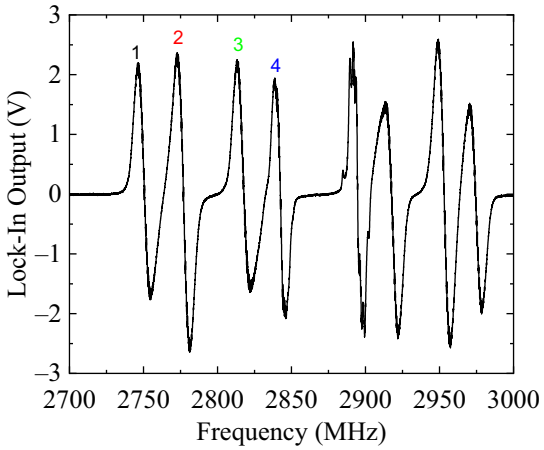

FIG. 8. The ODMR spectrum with the sensor head on the steel.

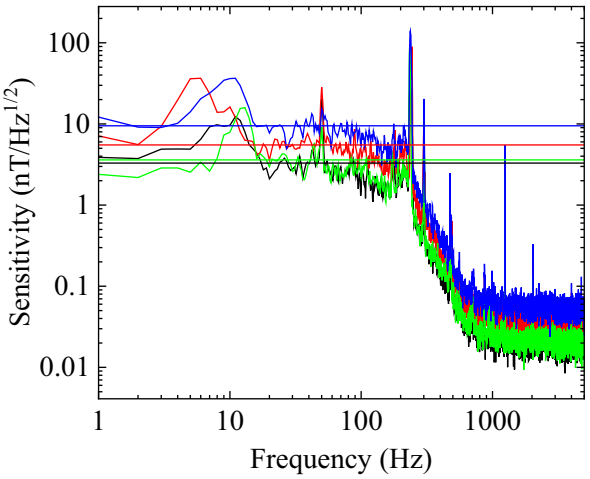

FIG. 9. Sensitivity for the four peaks while on the steel plate. The black, red, green, and blue traces correspond to the peaks labeled 1, 2, 3, and 4 in Fig. 2(a).

for each peak the shift in frequency was determined over the entire time trace. This shift in frequency was then used to calculate the B_{x}, B_{y}, and B_{z} values over the duration of the time trace and then for each axis the FFT for every second was taken and an average FFT was found, shown in Fig. 10. The mean average sensitivity for the components B_{x}, B_{y}, and B_{z} was 5.8 ± 3.6, 9.5 ± 5.1, and 3.8 ± 2.2 $\mathrm{nT}/\sqrt{\mathrm{Hz}}$, respectively.

Despite the high N-V density, high laser power, and large integration volume, the sensitivity is still of the order of $\mathrm{nT}/\sqrt{\mathrm{Hz}}$. This may be lower than expected, however, due to a number of factors. The introduction of the small bias magnet inside the sensor head causes broadening of the ODMR peaks due to a high inhomogeneous

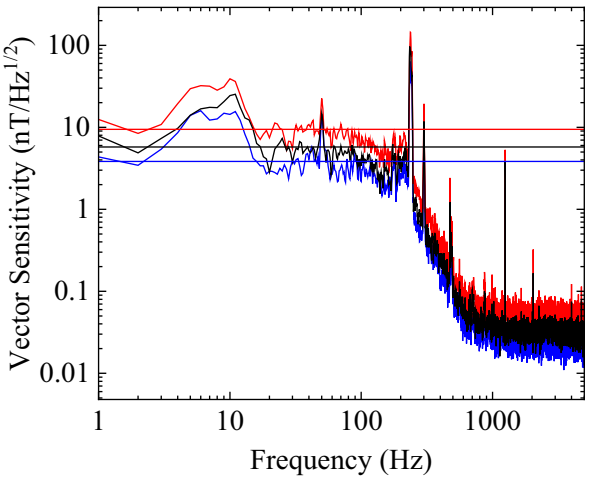

FIG. 10. Sensitivity of the three axes of the vector magnetometer (B_{x}, black; B_{y}, red; B_{z}, blue). The mean sensitivity between 10 and 100 Hz is shown by the horizontal lines.

field from the close proximity of the magnet to the diamond. This reduces the gradient of the ODMR peaks and therefore the sensitivity. A higher frequency modulation depth of 3 MHz was used to work with the resonance tracking to facilitate vector measurements, but such a high frequency-modulation depth can cause further broadening of the ODMR peaks, reducing sensitivity. The vector measurements required four well-separated ODMR peaks to measure the magnetic field projection along the four N-*V* center orientations in the diamond; however, this in turn means the sensitivity is reduced due to only being able to use a maximum of $\frac{1}{4}$ of the N-*V* population in that orientation, assuming 100% efficient spin polarization and MW addressing. It is likely that less than $\frac{1}{4}$ of the population is being addressed due to inefficiencies, further reducing sensitivity. Without these drawbacks, however, a sensitivity of 171 $\mathrm{pT}/\sqrt{\mathrm{Hz}}$ has been achieved with this same setup without sensor head scanning and vector measurement capabilities [66].

APPENDIX E: PARAMETER OPTIMIZATION

The parameters that yield the best sensitivity are found when the gradient of the ODMR peak is at a maximum and the noise floor is at a minimum. The parameter space was partially explored following the same procedure used in previous work [49,66], some of which follows theoretical modeling from El-Ella *et al.* [68]. The laser power during optimization was kept constant at 1 W. At each iteration of the parameters, the gradient and thirty 1-s FFTs of the fourth ODMR peak were taken to determine the sensitivity.

Firstly, the microwave power was increased from 0 to 43 dBm, as measured by a vector network analyzer after amplification, at the point where the microwaves were connected to the sensor head antenna. The modulation frequency and modulation deviation (also known as modulation amplitude) were kept constant at 3.0 kHz and 3.0 MHz, respectively. The sensitivity continued to increase with an increase in microwave power, as shown in Fig. 11 so a maximum power of 43 dBm was chosen. Even with this power, continuous running of the sensor head was possible without it overheating or damaging components. As a short is being driven, the radiated microwave power at the diamond is much less than 43 dBm. A resonator could improve the microwave power efficiency at the expense of limited bandwidth.

Next the optimum modulation frequency was found by increasing from 0.25 to 4.0 kHz in steps of 0.25 kHz. The microwave power and modulation deviation were kept constant at 43 dBm and 3.0 MHz, respectively. The optimum modulation frequency was found to be at 1.25 kHz, as shown in Fig. 12.

Lastly the modulation deviation was varied between 0.25 and 4.0 MHz. The microwave power and modulation frequency were kept constant at 43 dBm and 1.25 kHz, respectively. The optimum frequency deviation was found to be 2.0 MHz, as shown in Fig. 13.

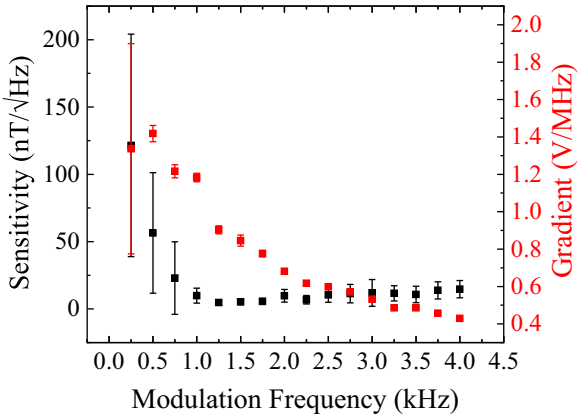

FIG. 12. The gradient of the ODMR peak and the sensitivity when on resonance for varying modulation frequency.

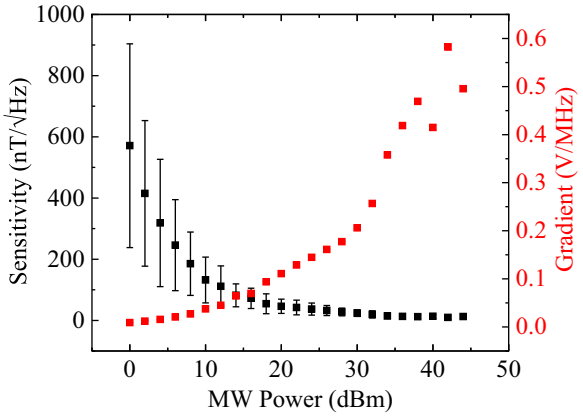

FIG. 11. The gradient of the ODMR peak and the sensitivity when on resonance for varying MW power.

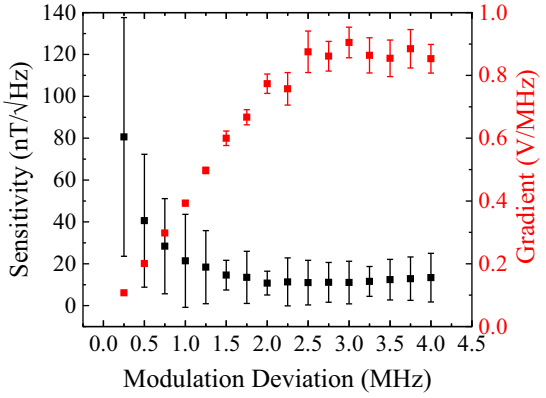

FIG. 13. The gradient of the ODMR peak and the sensitivity when on resonance for varying modulation deviation.

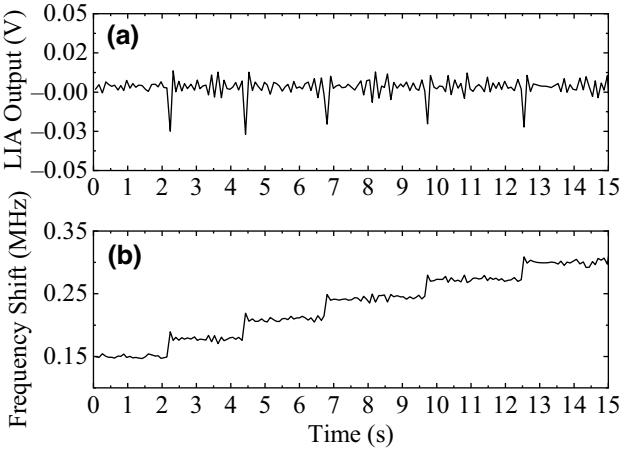

FIG. 14. (a) Frequency tracking of a single peak showing the lock-in amplifier output returning to its zero set point. (b) The microwave frequency changing in response to an applied magnetic field from a solenoid.

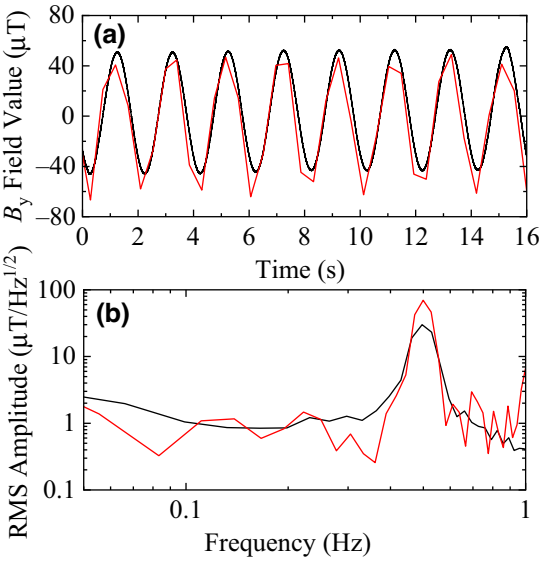

FIG. 15. (a) The tracked B_y field shift component measured by both the N-V magnetometer (red) and the fluxgate (black) for an applied 0.5-Hz field. (b) The FFT of the B_y field component time traces for both the N-V magnetometer (red) and the fluxgate (black) shown in (a).

APPENDIX F: RESONANCE LOCK

To significantly increase the dynamic range of the magnetometer, resonance tracking (also known as resonance locking) was introduced. This was done using a proportional linear feedback controller that every 50 ms would query the LIA output voltage and, given the gradient of the ODMR peak in V/MHz, would calculate how to change the microwave frequency and apply the error correction so to stay on the zero-crossing point of the peak. Figure 14 shows how the LIA output voltage is offset from its set point, due to a field provided by a solenoid coil around the sensor head, and then how it proceeds to return to its set point by increasing the microwave frequency.

When resonance locking was expanded to cover four ODMR peaks by applying the error correction to the first peak then moving onto the next peak, this process could be repeated every 400 ms, limited in refresh rate by the speed of the code executing and the time it took for the microwave source to process the commands. The estimated sampling rate from this is approximately 2 Hz.

APPENDIX G: ACCURACY TEST

To see how well our N-V vector magnetometer could accurately measure an applied external field in comparison with a commercially available Bartington Instruments Mag-03MS100 three-axis fluxgate magnetometer, a 0.5-Hz ac field was applied to the y sensing axis of both magnetometers. The solenoid used to apply the field has a calibration of 1.05 mT/A. The solenoid was calibrated using a Hall probe with 0.15-μT resolution. The signal generator generated a sine wave with a 10-V peak-to-peak amplitude with a peak current of approximately 50 mA. The expected peak field strength should be approximately 50 μT. The fluxgate has a sensitivity of 10 μT/V.

In Fig. 15(a) the time trace for the applied fields is shown. The fluxgate- and N-V-magnetometer-measured amplitudes were approximately 55 and 49 μT, respectively. These values match the expected field strength and also are in good agreement with each other.

To confirm that the resonance tracking could follow a 0.5-Hz signal well and also measure its strength correctly, when compared with the fluxgate, the FFT of the time traces was also taken as seen in Fig. 15(b). The FFT shows that both the fluxgate and the N-V magnetometer have similar peak amplitudes for the 0.5-Hz peak, which is present in both FFTs.

APPENDIX H: x AND y SPATIAL RESOLUTION

To determine the x and y spatial resolution, a scan was taken of another fresh 316 steel plate with holes drilled in it 10 mm apart with diameters of 0.7, 0.8, 0.9, 1, and 1.5 mm [Fig. 16(a)]. The holes were spaced 10 mm apart. The smallest hole diameter that could be seen was the 1.5-mm-diameter hole [Fig. 16(b)] so this was taken as the minimum x and y axis spatial resolution.

APPENDIX I: z-DIRECTION-DEPENDENT TENSOR COMPONENTS

To calculate the full gradient tensor, including the z-direction-dependent components, the sensor head was scanned in the x-y plane at two different heights to see

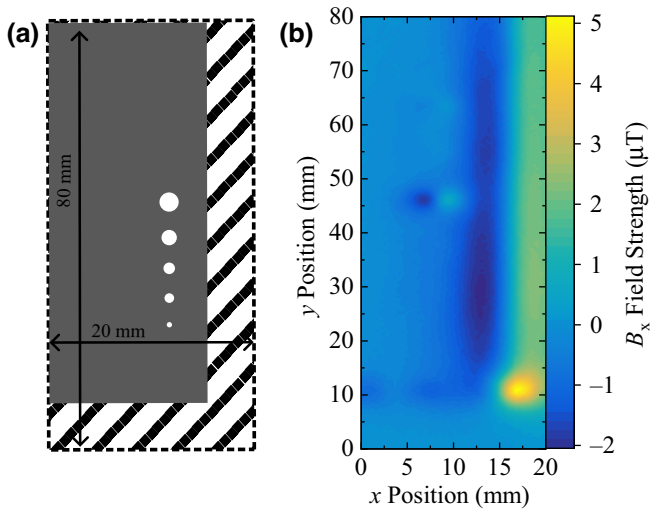

FIG. 16. (a) Diagram of the scanned area of the 316 stainless steel plate with varied hole diameters to test x and y spatial resolution. The holes are 0.7, 0.8, 0.9, 1, and 1.5 mm in diameter from bottom to top, respectively. The checkered area shows the scan region. (b) The B_x image of the same plate. Only the 1.5-mm-diameter hole is visible in the scan.

how the field changed in that direction. The sensor head was scanned at a height of 0.75 mm and 1 mm from the surface of the steel plate. The gradients of the x, y, and z components of the magnetic field were determined with respect to changes in the z direction and mapped as shown in Fig. 17. The maps did not provide much useful information as compared with the x and y components. A small change in separation between the sensor head and the sample causes a large change in the sensed magnetic field. This large change is thought to be due to the change in magnetic flux, from the small bias magnet, that flows through the material. Previous experiments have seen an approximately 40% change in LIA output voltage when doubling the distance from the sample [21]. Another cause of such a large shift could be due to the magnetic attraction between the small bias magnet in the sensor head and the steel plate. The attraction will be stronger when the sensor head and the magnet are closer to the steel sample, which will move the small bias magnet towards the steel plate. The movement relative to the diamond will cause a signal in the magnetometry measurements.

APPENDIX J: COMSOL SIMULATIONS

Simulations were performed using the COMSOL Inc. COMSOL Multiphysics software. COMSOL is finite-element modeling software. The simulations were run in the "Magnetic field, no current" mode. A 3D model steel plate [Fig. 18(a)] with the same dimensions as that used in the experiment [Fig. 18(b)] was created. Ten large 6-mm-diameter holes and 3 × 3 grid of 2-mm holes of varying depth were added to the steel plate geometry using cylinder shapes of the same size and length and the "difference" operation. The small (1 × 1 × 1)-mm^3 bias magnet was created by using a cube shape of the same size with N45 material. The small magnet was placed 1 mm from the surface of the steel plate, to reproduce the distance that the real bias magnet is from the hole during a scan. The N45 material gave the magnets a relative permeability of 1.05. The relative permeability of the stainless steel plate was set to 1.005, as this is typical for 316 stainless steel.

The north and south poles of the magnet were set to the top and bottom halves of the magnet, respectively [Fig. 18(c)]. To study how the magnetic field value changes for different bias field orientations, the small bias field was rotated 45° around its z axis [Fig. 18(d)] as well as being rotated 90° around its x axis and again rotated 45° [Figs. 18(e) and 18(f)]. This then turned the magnetic poles to be side to side rather than top to bottom.

To measure the magnetic field values, a two dimensional (2D) surface map was plotted using an x-y work plane that sliced through the steel plate at 1 mm below the surface. The B_x, B_y, and B_z field values as well as the total magnetic field surface maps were plotted for all the orientations of the small bias magnet investigated. The results are shown in Fig. 4(a) of the main paper.

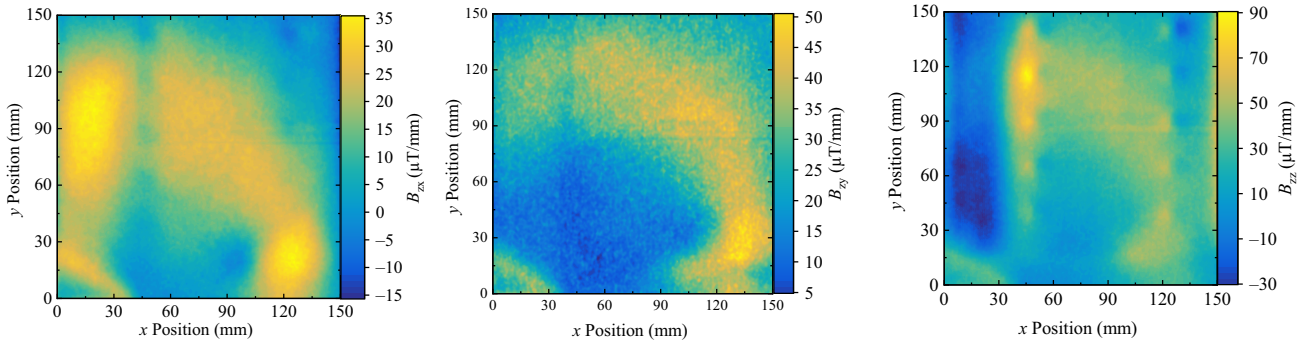

FIG. 17. Large changes in field are seen in the B_z-dependent gradient tensor components. These components were less useful for imaging as the holes could not be well resolved.

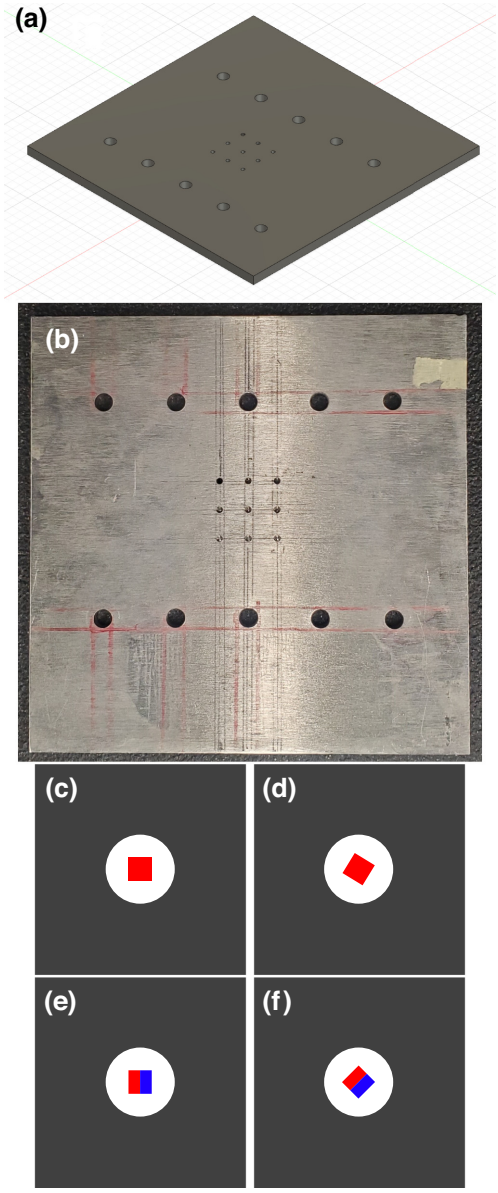

FIG. 18. (a) The 3D model of the stainless-steel plate used in the simulation. (b) A photo of the plate used in this study. (c) The small magnet above the hole with the north pole facing up. (d) The north pole rotated 45° around the z axis. (e) The magnet rotated 90° around the x axis, with the north and south poles going left to right. (f) The north and south poles now rotated 45°.

APPENDIX K: MAXWELL'S EQUATIONS

Constraints due to Maxwell's equations mean that only five of the nine magnetic gradient tensor components are independent. The divergence of the magnetic field is zero, meaning that the magnetic gradient tensor is traceless, which can be written as

$$B_{xx} + B_{yy} + B_{zz} = 0. \tag{K1}$$

Our experiment has no electric currents during the measurements and the electric fields are constant, so the curl of the magnetic field vector, $\vec{B}$, is equal to zero, $\nabla \times \vec{B} = 0$. In this situation, $\vec{B}$ can be expressed as the gradient of a scalar potential, Ω:

$$\vec{B} = \begin{pmatrix} B_x \\ B_y \\ B_z \end{pmatrix} = -\nabla\Omega = -\begin{pmatrix} \frac{\partial\Omega}{\partial x} \\ \frac{\partial\Omega}{\partial y} \\ \frac{\partial\Omega}{\partial z} \end{pmatrix}. \tag{K2}$$

By substituting this definition for the magnetic field vector into the magnetic gradient tensor [Eq. (1)], the magnetic gradient tensor can be expressed as

$$\begin{aligned} &-\begin{pmatrix} \frac{\partial}{\partial x}\left(\frac{\partial\Omega}{\partial x}\right) & \frac{\partial}{\partial x}\left(\frac{\partial\Omega}{\partial y}\right) & \frac{\partial}{\partial x}\left(\frac{\partial\Omega}{\partial z}\right) \\ \frac{\partial}{\partial y}\left(\frac{\partial\Omega}{\partial x}\right) & \frac{\partial}{\partial y}\left(\frac{\partial\Omega}{\partial y}\right) & \frac{\partial}{\partial y}\left(\frac{\partial\Omega}{\partial z}\right) \\ \frac{\partial}{\partial z}\left(\frac{\partial\Omega}{\partial x}\right) & \frac{\partial}{\partial z}\left(\frac{\partial\Omega}{\partial y}\right) & \frac{\partial}{\partial z}\left(\frac{\partial\Omega}{\partial z}\right) \end{pmatrix} \\ &= -\begin{pmatrix} \frac{\partial^2\Omega}{\partial x^2} & \frac{\partial^2\Omega}{\partial x\partial y} & \frac{\partial^2\Omega}{\partial x\partial z} \\ \frac{\partial^2\Omega}{\partial y\partial x} & \frac{\partial^2\Omega}{\partial y^2} & \frac{\partial^2\Omega}{\partial y\partial z} \\ \frac{\partial^2\Omega}{\partial z\partial x} & \frac{\partial^2\Omega}{\partial z\partial y} & \frac{\partial^2\Omega}{\partial z^2} \end{pmatrix}. \end{aligned} \tag{K3}$$

In a region with no current source, that is, that the current density and charge density do not change over time, the scalar potential and all its derivatives, including the magnetic field vector, are continuously differentiable. A continuously differentiable function, f , has a commutable partial derivative

$$\frac{\partial^2 f}{\partial x_i \partial x_j} = \frac{\partial^2 f}{\partial x_j \partial x_i}, \tag{K4}$$

where x_i is the respective Cartesian axes direction x, y, or z.

In the case of the continuously differentiable scalar potential function Ω,

$$\frac{\partial^2\Omega}{\partial x_i \partial x_j} = \frac{\partial^2\Omega}{\partial x_j \partial x_i}. \tag{K5}$$

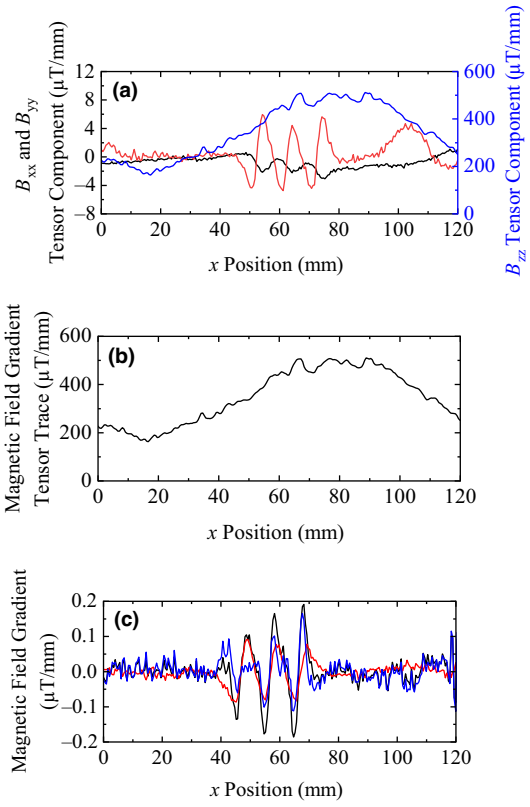

FIG. 19. (a) The trace components of the magnetic gradient tensor. Note the large difference in scale of the B_{xx} (black) and B_{yy} (red) components compared with the B_{zz} component (blue). (b) The trace of the magnetic tensor gradient. (c) The B_{xy} (black) and B_{yx} (red) tensor components along with their difference, $B_{xy} - B_{yx}$ (blue).

This implies

$$\frac{\partial^2\Omega}{\partial x\partial y} = \frac{\partial^2\Omega}{\partial y\partial x} = B_{xy} = B_{yx}, \tag{K6}$$

$$\frac{\partial^2\Omega}{\partial x\partial z} = \frac{\partial^2\Omega}{\partial z\partial x} = B_{xz} = B_{zx}, \tag{K7}$$

$$\frac{\partial^2\Omega}{\partial y\partial z} = \frac{\partial^2\Omega}{\partial z\partial y} = B_{yz} = B_{zy}. \tag{K8}$$

By comparing the difference between the magnetic gradient tensor component maps for the three conditions and by looking at the trace of the tensor we can check the consistency of these results by seeing how closely the results follow these conditions. However, the conditions (K1), (K6), (K7), and (K8) do not actually apply to our measurements because each magnetic gradient measurement was performed using two vector magnetic field measurements, with the small bias magnet moving in between the two measurements

By taking horizontal line profiles across the small holes in the center of the plate, looking at the diagonal components [Fig. 19(a)] and trace of the tensor [Fig. 19(b)] as well as the B_{xy} and B_{yx} difference [Fig. 19(c)], it can be determined how closely the measurements match the conditions described previously. From this it is clear to see that the trace of the tensor does not follow condition (K1) due to the large values of B_{zz}. The large values come from the large change in the measured z component of the B field at different scanning heights. The large difference is believed to be because the strength of the magnetic field inside the steel due to the small bias magnet inside the sensor head changes dramatically when moving in the z direction.

The difference between the B_{xy} and B_{yx} components shows that the two tensor components are similar away from the hole features but respond differently, and therefore give a large difference, near the holes. However, just as (K1) does not apply to our measurements, (K6)–(K8) also do not apply here. The conditions (K1), (K5), (K6), and (K7) would be more clearly seen for tensor gradiometry where four magnetic fields are measured without moving any bias magnets. The four magnetic fields would be a reference position and then one that is displaced in x, one that is displaced in y, and one that is displaced in z. The magnetic gradient tensor we measure has still shown to give good contrast and feature resolution when compared with vector measurements.

[1] M. Schiffler, M. Queitsch, R. Stolz, A. Chwala, W. Krech, H.-G. Meyer, and N. Kukowski, Calibration of squid vector magnetometers in full tensor gradiometry systems, Geophys. J. Int. **198**, 954 (2014).

[2] M. Luheshi, in *Integration of Geophysical Technologies in the Petroleum Industry*, edited by H. Wilson, K. Nunn, and M. Luheshi (Cambridge University Press, Cambridge, 2021), p. 124.

[3] K. Bisrat and M. Tilahun, Processing and interpretation of full tensor gravity anomalies of southern main Ethiopian rift, Heliyon **7**, e06872 (2021).

[4] R. Stolz, M. Schiffler, V. Zakosarenko, H. Larnier, J. Rudd, G. Chubak, L. Polomé, B. Pitts, M. Schneider, M. Schulz, M. Meyer, and K. Campbell, in *First International Meeting for Applied Geoscience; Energy Expanded Abstracts* (Society of Exploration Geophysicists (SEG), Denver, Colorado, USA, 2021), p. 3554.

[5] L. B. Pedersen and T. M. Rasmussen, The gradient tensor of potential field anomalies: Some implications on data collection and data processing of maps, Geophys **55**, 1558 (1990).

[6] C. Foss, Improvements in source resolution that can be expected from inversion of magnetic field tensor data, Lead. Edge **25**, 81 (2006).

[7] A. Chwala, R. Stolz, V. Zakosarenko, L. Fritzsch, M. Schulz, A. Rompel, L. Polome, M. Meyer, and H. G. Meyer, Full tensor squid gradiometer for airborne exploration, ASEG **2012**, 1 (2012).

[8] A. A. Wood, L. M. Bennie, A. Duong, M. Jasperse, L. D. Turner, and R. P. Anderson, Magnetic tensor gradiometry using Ramsey interferometry of spinor condensates, Phys. Rev. A **92**, 053604 (2015).

[9] S. T. Keenan, D. A. Clark, and K. E. Leslie, Method for full magnetic gradient tensor detection from a single HTS gradiometer, Supercond. Sci. Technol. **35**, 045005 (2022).

[10] P. W. Schmidt and D. A. Clark, The magnetic gradient tensor: Its properties and uses in source characterization, Lead. Edge **25**, 75 (2006).

[11] P. Schmidt, D. Clark, K. Leslie, M. Bick, D. Tilbrook, and C. Foley, GETMAG—A SQUID magnetic tensor gradiometer for mineral and oil exploration, Explor. Geophys. **35**, 297 (2004).

[12] C. A. Murphy and J. Brewster, Target delineation using full tensor gravity gradiometry data, ASEG Ext. Abstr. **2007**, 1 (2007).

[13] J. M. Schloss, J. F. Barry, M. J. Turner, and R. L. Walsworth, Simultaneous broadband vector magnetometry using solid-state spins, Phys. Rev. Appl. **10**, 34044 (2018).

[14] Y. Luo, M. P. Wu, P. Wang, S. L. Duan, H. J. Liu, J. L. Wang, and Z. F. An, Full magnetic gradient tensor from triaxial aeromagnetic gradient measurements: Calculation and application, Appl. Geophys. **12**, 283 (2015).

[15] K. Kubota, Y. Hatano, Y. Kainuma, J. Shin, D. Nishitani, C. Shinei, T. Taniguchi, T. Teraji, S. Onoda, T. Ohshima, T. Iwasaki, and M. Hatano, Wide temperature operation of diamond quantum sensor for electric vehicle battery monitoring, Diamond Relat. Mater. **135**, 109853 (2023).

[16] Y. Hatano, J. Shin, D. Nishitani, H. Iwatsuka, Y. Masuyama, H. Sugiyama, M. Ishii, S. Onoda, T. Ohshima, K. Arai, T. Iwasaki, and M. Hatano, Simultaneous thermometry and magnetometry using a fiber-coupled quantum diamond sensor, Appl. Phys. Lett. **118**, 034001 (2021).

[17] B. Zuo, L. Wang, and W. Chen, Full tensor eigenvector analysis on air-borne magnetic gradiometer data for the detection of dipole-like magnetic sources, Sensors **17**, 1976 (2017).

[18] Y. Gang, Z. Yingtang, F. Hongbo, R. GuoQuan, and L. Zhining, Integrated calibration of magnetic gradient tensor system, J. Magn. Magn. Mater. **374**, 289 (2015).

[19] Y. Gang, Z. Yingtang, L. Zhining, F. Hongbo, and R. Guoquan, Detection of ferromagnetic target based on mobile magnetic gradient tensor system, J. Magn. Magn. Mater. **402**, 1 (2016).

[20] J. A. Young and D. A. Clark, in *2010 International Conference on Electromagnetics in Advanced Applications* (Institute of Electrical and Electronics Engineers (IEEE), Sydney, Australia, 2010), p. 701.

[21] L. Q. Zhou, R. L. Patel, A. C. Frangeskou, A. Nikitin, B. L. Green, B. G. Breeze, S. Onoda, J. Isoya, and G. W. Morley, Imaging damage in steel using a diamond magnetometer, Phys. Rev. Appl. **15**, 24015 (2021).

[22] M. W. Dale and G. W. Morley, Medical applications of diamond magnetometry: Commercial viability, ArXiv:1705.01994 (2017).

[23] R. L. Fagaly, Superconducting quantum interference device instruments and applications, Rev. Sci. Instrum. **77**, 101101 (2006).

[24] R. Körber *et al.* SQUIDs in biomagnetism: A roadmap towards improved healthcare, Supercond. Sci. Technol. **29**, 113001 (2016).

[25] M. H. Acuña, Space-based magnetometers, Rev. Sci. Instrum. **73**, 3717 (2002).

[26] C. J. Cochrane, J. Blacksberg, M. A. Anders, and P. M. Lenahan, Vectorized magnetometer for space applications using electrical readout of atomic scale defects in silicon carbide, Sci. Rep. **6**, 37077 (2016).

[27] E. Boto, N. Holmes, J. Leggett, G. Roberts, V. Shah, S. S. Meyer, L. D. Muñoz, K. J. Mullinger, T. M. Tierney, S. Bestmann, G. R. Barnes, R. Bowtell, and M. J. Brookes, Moving magnetoencephalography towards real-world applications with a wearable system, Nature **555**, 657 (2018).

[28] M. Jiang, R. P. Frutos, T. Wu, J. W. Blanchard, X. Peng, and D. Budker, Magnetic gradiometer for the detection of zero- to ultralow-field nuclear magnetic resonance, Phys. Rev. Appl. **11**, 024005 (2019).

[29] N. A. Hoult, O. Ekim, and R. Regier, Damage/deterioration detection for steel structures using distributed fiber optic strain sensors, J. Eng. Mech. **140**, 4014097 (2014).

[30] M. P. Paulraj, S. Yaacob, M. S. A. Majid, M. N. F. M. Kazim, and P. Krishnan, Structural steel plate damage detection using non destructive testing, frame energy based statistical features and artificial neural networks, Proc. Eng. **53**, 376 (2013).

[31] M. Hu, J. He, C. Zhou, Z. Shu, and W. Yang, Surface damage detection of steel plate with different depths based on Lamb wave, Measurement **187**, 110364 (2022).

[32] V. Suresh, A. Abudhahir, and J. Daniel, Development of magnetic flux leakage measuring system for detection of defect in small diameter steam generator tube, Measurement **95**, 273 (2017).

[33] H. Kikuchi, Y. Kurisawa, K. Ara, Y. Kamada, and S. Kobayashi, Feasibility study of magnetic flux leakage method for condition monitoring of wall thinning on tube, Int. J. Appl. Electromagn. **33**, 1087 (2010).

[34] H. Kikuchi, K. Sato, I. Shimizu, Y. Kamada, and S. Kobayashi, Feasibility study of application of MFL to monitoring of wall thinning under reinforcing plates in nuclear power plants, IEEE Trans. Magn. **47**, 3963 (2011).

[35] X. Peng, U. Anyaoha, Z. Liu, and K. Tsukada, Analysis of magnetic-flux leakage (MFL) data for pipeline corrosion assessment, IEEE Trans. Magn. **56**, 1 (2020).

[36] B. Liu, L. He, H. Zhang, Y. Cao, and H. Fernandes, The axial crack testing model for long distance oil-gas pipeline based on magnetic flux leakage internal inspection method, Measurement **103**, 275 (2017).

[37] B. Campbell and A. Mainwood, Radiation damage of diamond by electron and gamma irradiation, Phys. Status Solidi A **181**, 99 (2000).

[38] B. Campbell, W. Choudhury, A. Mainwood, M. Newton, and G. Davies, Lattice damage caused by the irradiation of diamond, Nucl. Instrum. Methods Phys. Res. A **476**, 680 (2002).

[39] T. Behnke, M. Doucet, N. Ghodbane, A. Imhof, C. Martínez, and W. Zeuner, Electromagnetic radiation hardness of diamond detectors, Nucl. Instrum. Methods Phys. Res. A **489**, 230 (2002).

[40] J. F. Barry, J. M. Schloss, E. Bauch, M. J. Turner, C. A. Hart, L. M. Pham, and R. L. Walsworth, Sensitivity optimization for NV-diamond magnetometry, Rev. Mod. Phys. **92**, 15004 (2020).

[41] J. M. Taylor, P. Cappellaro, L. Childress, L. Jiang, D. Budker, P. R. Hemmer, A. Yacoby, R. Walsworth, and M. D. Lukin, High-sensitivity diamond magnetometer with nanoscale resolution, Nat. Phys. **4**, 810 (2008).

[42] V. M. Acosta, E. Bauch, M. P. Ledbetter, C. Santori, K.-M. C. Fu, P. E. Barclay, R. G. Beausoleil, H. Linget, J. F. Roch, F. Treussart, S. Chemerisov, W. Gawlik, and D. Budker, Diamonds with a high density of nitrogen-vacancy centers for magnetometry applications, Phys. Rev. B **80**, 115202 (2009).

[43] T. Plakhotnik, M. W. Doherty, J. H. Cole, R. Chapman, and N. B. Manson, All-optical thermometry and thermal properties of the optically detected spin resonances of the NV– center in nanodiamond, Nano Lett. **14**, 4989 (2014).

[44] D. M. Toyli, D. J. Christle, A. Alkauskas, B. B. Buckley, C. G. Van de Walle, and D. D. Awschalom, Measurement and control of single nitrogen-vacancy center spins above 600 K, Phys. Rev. X **2**, 31001 (2012).

[45] D. M. Toyli, C. F. de las Casas, D. J. Christle, V. V. Dobrovitski, and D. D. Awschalom, Fluorescence thermometry enhanced by the quantum coherence of single spins in diamond, Proc. Natl. Acad. Sci. USA **110**, 8417 (2013).

[46] M. W. Doherty, N. B. Manson, P. Delaney, F. Jelezko, J. Wrachtrup, and L. C. L. Hollenberg, The nitrogen-vacancy colour centre in diamond, Phys. Rep. **528**, 1 (2013).

[47] S. Hsieh, P. Bhattacharyya, C. Zu, T. Mittiga, T. J. Smart, F. Machado, B. Kobrin, T. O. Höhn, N. Z. Rui, M. Kamrani, S. Chatterjee, S. Choi, M. Zaletel, V. V. Struzhkin, J. E. Moore, V. I. Levitas, R. Jeanloz, and N. Y. Yao, Imaging stress and magnetism at high pressures using a nanoscale quantum sensor, Science **366**, 1349 (2019).

[48] V. Ivády, T. Simon, J. R. Maze, I. A. Abrikosov, and A. Gali, Pressure and temperature dependence of the zero-field splitting in the ground state of NV centers in diamond: A first-principles study, Phys. Rev. B **90**, 235205 (2014).

[49] S. M. Graham, A. T. M. A. Rahman, L. Munn, R. L. Patel, A. J. Newman, C. J. Stephen, G. Colston, A. Nikitin, A. M. Edmonds, D. J. Twitchen, M. L. Markham, and G. W. Morley, Fiber-coupled diamond magnetometry with an unshielded sensitivity of 30 $\mathrm{pT}/\sqrt{\mathrm{Hz}}$, Phys. Rev. Appl. **19**, 044042 (2023).

[50] S.-C. Zhang, H.-B. Lin, Y. Dong, B. Du, X.-D. Gao, C. Yu, Z.-H. Feng, X.-D. Chen, G.-C. Guo, and F.-W. Sun, High-sensitivity and wide-bandwidth fiber-coupled diamond magnetometer with surface coating, Photonics Res. **10**, 2191 (2022).

[51] G. Chatzidrosos, A. Wickenbrock, L. Bougas, H. Zheng, O. Tretiak, Y. Yang, and D. Budker, Eddy-current imaging with nitrogen-vacancy centers in diamond, Phys. Rev. Appl. **11**, 14060 (2019).

[52] M. I. Ibrahim, C. Foy, D. Kim, D. R. Englund, and R. Han, in *2018 IEEE Symposium on VLSI Circuits* (Institute of Electrical and Electronics Engineers (IEEE), Honolulu, Hawaii, USA, 2018), p. 249.

[53] C. Xu, J. Zhang, H. Yuan, G. Bian, P. Fan, M. Li, and T. Liu, Burst eddy current testing with diamond magnetometry, Appl. Phys. Lett **120**, 084104 (2022).

[54] J. F. Barry, M. J. Turner, J. M. Schloss, D. R. Glenn, Y. Song, M. D. Lukin, H. Park, and R. L. Walsworth, Optical magnetic detection of single-neuron action potentials using quantum defects in diamond, Proc. Natl. Acad. Sci. USA **113**, 14133 (2016).

[55] A. Kuwahata, T. Kitaizumi, K. Saichi, T. Sato, R. Igarashi, T. Ohshima, Y. Masuyama, T. Iwasaki, M. Hatano, F. Jelezko, M. Kusakabe, T. Yatsui, and M. Sekino, Magnetometer with nitrogen-vacancy center in a bulk diamond for detecting magnetic nanoparticles in biomedical applications, Sci. Rep. **10**, 2483 (2020).

[56] H. C. Davis, P. Ramesh, A. Bhatnagar, A. Lee-Gosselin, J. F. Barry, D. R. Glenn, R. L. Walsworth, and M. G. Shapiro, Mapping the microscale origins of magnetic resonance image contrast with subcellular diamond magnetometry, Nat. Commun. **9**, 131 (2018).

[57] X. Liu, J. Cui, F. Sun, X. Song, F. Feng, J. Wang, W. Zhu, L. Lou, and G. Wang, Fiber-integrated diamond-based magnetometer, Appl. Phys. Lett. **103**, 143105 (2013).

[58] A. K. Dmitriev and A. K. Vershovskii, Concept of a microscale vector magnetic field sensor based on nitrogen-vacancy centers in diamond, J. Opt. Soc. Am. B **33**, B1 (2016).

[59] F. M. Stürner, A. Brenneis, T. Buck, J. Kassel, R. Rölver, T. Fuchs, A. Savitsky, D. Suter, J. Grimmel, S. Hengesbach, M. Förtsch, K. Nakamura, H. Sumiya, S. Onoda, J. Isoya, and F. Jelezko, Integrated and portable magnetometer based on nitrogen-vacancy ensembles in diamond, Adv. Quantum Technol. **4**, 2000111 (2021).

[60] G. Chatzidrosos, J. S. Rebeirro, H. Zheng, M. Omar, A. Brenneis, F. M. Stürner, T. Fuchs, T. Buck, R. Rölver, T. Schneemann, P. Blümler, D. Budker, and A. Wickenbrock, Fiberized diamond-based vector magnetometers, Front. Phys. **2**, 4 (2021).

[61] F. Xie, Q. Liu, Y. Hu, L. Li, Z. Chen, J. Zhang, Y. Zhang, Y. Zhang, Y. Wang, J. Cheng, H. Chen, and Z. Wu, in *2023 IEEE 36th International Conference on Micro Electro Mechanical Systems (MEMS)* (Institute of Electrical and Electronics Engineers (IEEE), Munich, Germany, 2023), p. 157.

[62] J. Shao, Y. Luo, J. Chen, H. Huang, G.-S. Liu, L. Chen, Z. Chen, and Y. Chen, High-sensitivity optical-fiber magnetic sensor based on diamond and magnetic flux concentrators, Opt. Express **31**, 14685 (2023).

[63] Y. Masuyama, K. Suzuki, A. Hekizono, M. Iwanami, M. Hatano, T. Iwasaki, and T. Ohshima, Gradiometer using separated diamond quantum magnetometers, Sensors **21**, 977 (2021).

[64] S. M. Blakley, I. V. Fedotov, L. V. Amitonova, E. E. Serebryannikov, H. Perez, S. Ya. Kilin, and A. M. Zheltikov, Fiber-optic vectorial magnetic-field gradiometry by a spatiotemporal differential optical detection of magnetic resonance in nitrogen–vacancy centers in diamond, Opt. Lett. **41**, 2057 (2016).

[65] A. M. Edmonds, C. A. Hart, M. J. Turner, Pierre-Oliviers C. J. M. Schloss, K. S. Olsson, R. Trubko, M. L. Markham, A. Rathmill, B. Horne-Smith, W. Lew, A. Manickam, S. Bruce, P. G. Kaup, J. C. Russo, M. J. DiMario, J. T.

South, J. T. Hansen, D. J. Twitchen, and R. L. Walsworth, Characterisation of CVD diamond with high concentrations of nitrogen for magnetic-field sensing applications, Mater. Quantum Technol. **1**, 025001 (2021).

[66] R. L. Patel, L. Q. Zhou, A. C. Frangeskou, G. A. Stimpson, B. G. Breeze, A. Nikitin, M. W. Dale, E. C. Nichols, W. Thornley, B. L. Green, M. E. Newton, A. M. Edmonds, M. L. Markham, D. J. Twitchen, and G. W. Morley, Subnanotesla magnetometry with a fiber-coupled diamond sensor, Phys. Rev. Appl. **14**, 44058 (2020).

[67] S. Sengottuvel, M. Mrózek, M. Sawczak, M. J. Głowacki, M. Ficek, W. Gawlik, and A. M. Wojciechowski, Wide-field magnetometry using nitrogen-vacancy color centers with randomly oriented micro-diamonds, Sci. Rep. **12**, 17997 (2022).

[68] H. A. R. El-Ella, S. Ahmadi, A. M. Wojciechowski, A. Huck, and U. L. Andersen, Optimised frequency modulation for continuous-wave optical magnetic resonance sensing using nitrogen-vacancy ensembles, Opt. Express **25**, 14809 (2017).